Proceedings of ASME Turbo Expo 2011
GT2011
June 6-10, 2011, Vancouver, British Columbia, Canada

GT2011-45749

LARGE-EDDY SIMULATION WITH ZONAL NEAR WALL TREATMENT OF FLOW AND HEAT TRANSFER IN A RIBBED DUCT FOR THE INTERNAL COOLING OF TURBINE BLADES

Sunil Patil
Virginia Tech
Blacksburg, Virginia, USA

Danesh Tafti
Virginia Tech
Blacksburg, Virginia, USA

ABSTRACT

Large eddy simulations of flow and heat transfer in a square ribbed duct with rib height to hydraulic diameter of 0.1 and 0.05 and rib pitch to rib height ratio of 10 and 20 are carried out with the near wall region being modeled with a zonal two layer model. A novel formulation is used for solving the turbulent boundary layer equation for the effective tangential velocity in a generalized co-ordinate system in the near wall zonal treatment. A methodology to model the heat transfer in the zonal near wall layer in the LES framework is presented. This general approach is explained for both Dirichlet and Neumann wall boundary conditions. Reynolds numbers of 20,000 and 60,000 are investigated. Predictions with wall modeled LES are compared with the hydrodynamic and heat transfer experimental data of Rau et al. [1], and Han et al. [2], and wall resolved LES data of Tafti [3]. Friction factor, heat transfer coefficient, mean flow as well as turbulent statistics match available data closely with very good accuracy. Wall modeled LES at high Reynolds numbers as presented in this paper reduces the overall computational complexity by factors of 60-140 compared to resolved LES, without any significant loss in accuracy.

1 INTRODUCTION

Ribbed internal cooling duct configurations are used extensively in modern gas turbine engines. Ribs or turbulators act as roughness elements enhancing the heat transfer coefficient and cooling capacity. Flow in these ribbed ducts involves many complex features like flow separation, curved shear layers, primary and secondary recirculation, reattachment of the boundary layer and recovery. Rotation of turbine blades introduces Coriolis forces while high thermal gradients introduce centrifugal buoyancy. In the past two decades, several experimental studies have been performed to characterize the heat transfer in rib roughened passages. Several researchers at Texas A&M (Han [4, 5], Chandra et al. [6], Lau et al. [7], Han and Zhang [8], Han et al. [9], Zhang et al. [10], Ekkad and Han [11]) have studied the effects of different rib angles, different rib orientations, full and discrete ribs, different rib height/hydraulic diameter ratios, different rib pitch/height ratios, different aspect ratio channels, and variable temperature and flux boundary condition in a Reynolds number range from 10,000 to 100,000. Taslim et al. [12], Korotky and Taslim [13], Taslim and Lengknong [14], Taslim and Korotky [15] have performed similar studies.

Many researchers have reported computational studies on the internal cooling channels. Many of these studies relied heavily on the RANS approach for modeling turbulence. Saidi and Sunden [16], Jia et al. [17], Iacovides et al. [18], Ooi et al. [19] and Prakash and Zerkle [20] have performed three dimensional RANS calculations on stationary ducts while Jang et al. [21], Chen et al. [22], and Iacovides et al. [23] carried out RANS studies on rotating ducts. Due to the anisotropic nature of the turbulent flow in these ribbed internal cooling passages the investigated RANS models have had varying degree of success. The models based on eddy-viscosity [20], which assume flow isotropy do not perform well, while more complex models, which solve for the Reynolds stresses [17, 21, 24] have been found to perform reasonably well. RANS based models also suffer from lack of repeatability and low level of accuracy in predicting complex flow features in ribbed internal cooling ducts. Though computational expense has limited most studies to the RANS approach, in recent years, significant numbers of researchers have reported large-eddy simulation in internal cooling passages. LES has the potential to predict results more accurately by modeling only the small isotropic scales while resolving most of the energy containing eddies. Murata and Mochizuki [25] reported a LES calculation of a stationary duct for low Reynolds number without any experimental validation. Excellent comparisons between LES calculations and experiments have been shown in fully developed stationary ducts by Tafti [2], in fully developed rotating ducts by Abdel-Wahab and Tafti [26], in fully developed stationary ducts with 45^o ribs by Abdel-Wahab and Tafti [27], and in developing flow in stationary and rotating ducts by Sewall and Tafti [28].

Though many LES calculations have been reported in the literature, most of them are limited to either a fully developed assumption or to low Reynolds numbers, while most of the gas turbine applications have high operating Reynolds numbers. Although LES only resolves the large-scale unsteady flow dynamics in complex flows, it requires large computational resources at practical Reynolds number, which are of order of several hundred thousand. Resolution requirements near the wall increase tremendously with Reynolds number [29]. Also, it is important to note that the time step of the whole calculation is usually constrained by the smallest grid size. Hence, it is crucial to reduce the high resolution requirement for successful implementation of LES at high Reynolds numbers. Modeling the near wall region and coupling it to the outer LES region is key to the use of LES for practical engineering applications.

Three approaches for modeling the near wall layer are, use of logarithmic law of the wall based functions, solving a separate set of equations in the near-wall region, and simulating this region in a Reynolds-averaged sense. Deardorff [30] and Schumann [31] introduced approximate wall-boundary conditions to model the effect of the near wall layer. Grotzbach [32], Werner and Wengle [33], Piomelli et al. [34], Hoffmann and Benocci [35], and Temmerman et al. [36] used different variants of this approach. The major drawback of this approach is that it needs a value of mean wall shear stress *a priori* and the plane averaged velocity at the first grid point off the wall has to explicitly satisfy the logarithmic law of the wall. Hence, Schumann's [31] model and its variants work well only in simple equilibrium flows like the fully developed channel and pipe flows.

In recent years, hybrid RANS-LES approach has caught the attention of many researchers in which RANS equations are solved near the wall while the LES filtered Navier-Stokes equations are solved away from the wall. Various methodologies are used to switch between the RANS and LES. Spalart et al. [37] proposed Detached Eddy Simulation (DES) for separated flows in which a characteristic turbulent length scale was used as a criterion to switch between the RANS and LES regions. Nikitin et al. [38] used Spalart et al. [37] model and found significant under prediction in the wall shear stress. Vishwanathan and Tafti [39] carried out DES of fully developed flow and heat transfer in a internal cooling ribbed duct geometry. These hybrid RANS-LES models have the capability to simulate complex flows but still suffer from a high grid resolution requirement in the wall normal direction, which require $y^+<1$. Compatibility of the turbulence conditions at the interface and aliasing effects due to the resolved and modeled turbulence are major challenges in this method [40].

The zonal model or two-layer model (TLM) on the other hand solves a different set of equations in the inner layer [41]. Simplified turbulent boundary layer equations are solved on a virtual grid set up in the wall layer. This grid is embedded in the outer LES grid and refined only in the wall normal direction. In the outer LES grid, the filtered Navier-Stokes equations are solved, while in the inner layer Equation (1) is solved on a virtual grid embedded between the first grid point off the wall and the wall.

$$\frac{\partial \overline{u}_i}{\partial t} + \frac{\partial}{\partial x_i}\left(\overline{u}_n \overline{u}_i\right) = -\frac{\partial \overline{p}}{\partial x_i} + \frac{\partial}{\partial x_n}\left[\left(\upsilon + \upsilon_t\right)\frac{\partial \overline{u}_i}{\partial x_n}\right] \qquad (1)$$

In Equation (1), n is the wall normal direction and i takes values 1,2 or 1,3 based on the wall orientation. Equation (1) is solved using the no-slip boundary condition at the wall, and the velocity at the first grid point off the wall, which is calculated from the outer-flow LES. Balaras and Benocci [41] and Balaras et al. [42] used an algebraic eddy viscosity model to parameterize all scales of motion in the wall layer. The zonal model is discussed in more detail in the next section. The zonal approach has been successfully applied to a variety of problems in recent years. Cabot and Moin [43] simulated the flow over a backward facing step, Wang and Moin [44] studied flow past an asymmetric trailing edge and Tessicini et al. [45] simulated the three-dimensional flow around a hill-shaped obstruction with the zonal near wall approach. In all these applied schemes, turbulent boundary layer equations are solved in the inner layer virtual mesh to obtain the instantaneous wall shear stress, which is fed back as a boundary condition to the outer LES region.

Most of the applications of wall layer modeling in LES framework have been applied to fluid flow problems without heat transfer. In the current study, zonal treatment for the near wall heat transfer for coarser meshes is presented. The zonal two layer model for velocity and temperature is integrated and formulated to account for Dirichlet as well as Neumann thermal boundary conditions at the wall. A thorough validation of the proposed formulation is done in a fully developed turbulent channel flow with a specified heat flux against wall resolved LES calculations. This validated methodology is then applied to investigate the fully developed flow and heat transfer in a square ribbed duct used in gas turbine bade cooling. Two different configurations are studied with ratio of rib height to hydraulic diameter of 0.1 and 0.05 and rib pitch to rib height ratio of 10 and 20. Reynolds numbers based on the hydraulic diameter of the duct and bulk mean velocity were 20,000 and 60,000 respectively for these two configurations. Predictions with the wall modeled LES calculations are compared with the available experimental data of Rau et al. [1], Han et al. [2], and wall resolved LES data of Tafti [3] for Reynolds number of 20,000. It is observed that these LES calculations with zonal treatment for velocity and temperature are able to reproduce the major flow features in the duct. Also, the trends in the surface heat transfer coefficient and values of Nusselt augmentation were predicted in close agreement with the experimental measurements. It is also shown that in this complex flow, in the absence of wall modeling, on a coarse near wall grid, significant under prediction of friction factor and Nusselt number occur. This is first of a kind study where a statistically three dimensional flow is studied with heat transfer using an integrated zonal near wall treatment for both velocity and temperature in a generalized coordinate LES framework.

2 COMPUTATIONAL METHODOLOGY

2.1 Governing equations

The governing equations for unsteady incompressible viscous flow in a generalized coordinate system consists of mass, momentum, and energy conservation laws. The equations are mapped from physical $(\vec{x})$ to logical/computational space $(\vec{\xi})$ by a boundary conforming transformation $\vec{x} = \vec{x}(\vec{\xi})$, where $\vec{x} = (x, y, z)$ and $\vec{\xi} = (\xi, \eta, \zeta)$. The equations are non-dimensionalized by a suitable length scale ($L^*=D_h$), velocity scale ($U^*=u_\tau$) and a temperature scale ($q''_w L^*/k$), where q''_w is the heat flux at the wall. The modified equations, in which pressure and temperature are decomposed into mean and fluctuating or periodic components, are written in conservative nondimensional form as:

Mass:

$$\frac{\partial}{\partial \xi_j}\left(\sqrt{g} U^j\right) = 0 \tag{2}$$

Momentum

$$\frac{\partial}{\partial t}\left(\sqrt{g} u_i\right) + \frac{\partial}{\partial \xi_j}\left(\left(\sqrt{g} U^j\right) u_i\right) = -\frac{\partial}{\partial \xi_j}\left(\sqrt{g}\,(\vec{a}^{\,j})_i\, p\right) + \frac{\partial}{\partial \xi_j}\left(\left(\frac{1}{\mathrm{Re}} + \frac{1}{\mathrm{Re}_t}\right)\sqrt{g}\, g^{jk} \frac{\partial u_i}{\partial \xi_k}\right) + \sqrt{g}\,\beta \delta_{i1} \tag{3}$$

Energy

$$\frac{\partial}{\partial t}\left(\sqrt{g}\,\theta\right) + \frac{\partial}{\partial \xi_j}\left(\left(\sqrt{g} U^j\right)\theta\right) = \frac{\partial}{\partial \xi_j}\left(\left(\frac{1}{\mathrm{Re}\,\mathrm{Pr}} + \frac{1}{\mathrm{Re}_t\,\mathrm{Pr}_t}\right)\sqrt{g}\, g^{jk} \frac{\partial u_i}{\partial \xi_k}\right) - \sqrt{g}\,\gamma u_1 \tag{4}$$

where $\vec{a}^{\,i}$ are the contravariant basis vectors, $\sqrt{g}$ is the Jacobian of the transformation, g^{ij} is the contravariant metric tensor, $\sqrt{g} U^j = \sqrt{g}\left(\vec{a}^{\,j}\right)_k u_k$ is the contravariant flux vector, u_i is the Cartesian velocity vector, p is the pressure, and θ is the non-dimensional temperature. The non-dimensional time used is t^*U^*/L^* and the Reynolds number is given by U^*L^*/ν, Re_t is the inverse of the subgrid eddy-viscosity, which is modeled as

$$\frac{1}{\mathrm{Re}_t} = C_s^{\,2}(\sqrt{g})^{2/3}\left|\overline{S}\right| \tag{5}$$

where $\left|\overline{S}\right|$ is the magnitude of the strain rate tensor given by $\left|\overline{S}\right| = \sqrt{2\overline{S_{ik}}\,\overline{S_{ik}}}$ and the Smagorinsky constant $C_s^{\,2}$ is obtained via the dynamic subgrid stress model [46]. To this end, a second test filter, denoted by $\hat{G}$, is applied to the filtered governing equations with the characteristic length scale of $\hat{G}$ being larger than that of the grid filter, $\overline{G}$. The test filtered quantity is obtained from the grid filtered quantity by a second-order trapezoidal filter, which is given by $\hat{\varphi} = \frac{1}{4}(\overline{\varphi}_{i-1} + 2\overline{\varphi}_i + \overline{\varphi}_{i+1})$ in one dimension. The resolved turbulent stresses, representing the energy scales between the test and grid filters, $L_{ij} = \widehat{\overline{u}_i\overline{u}_j} - \hat{\overline{u}}_i\hat{\overline{u}}_j$, are then related to the subtest, $T_{ij} = \widehat{\overline{u_i u_j}} - \hat{\overline{u}}_i\hat{\overline{u}}_j$, and subgrid-scales stresses $\tau_{ij} = \overline{u_i u_j} - \overline{u}_i\overline{u}_j$ through the identity, $L_{ij}^a = T_{ij}^a - \hat{\tau}_{ij}^a$. The anisotropic subgrid and subtest-scale stresses are then formulated in terms of the Smagorinsky eddy viscosity model as:

$$\widehat{\tau_{ij}^a} = -2C_s^2\left(\sqrt{g}\right)^{2/3}\widehat{\left|\overline{S}\right|\overline{S_{ij}}} \tag{6}$$

$$T_{ij}^a = -2C_s^{\,2}\alpha\left(\sqrt{g}\right)^{2/3}\left|\hat{\overline{S}}\right|\widehat{\overline{S_{ij}}} \tag{7}$$

using the identity,

$$\begin{aligned}\widehat{L_{ij}^a} &= \widehat{L}_{ij} - \frac{1}{3}\delta_{ij}L_{kk} = 2C_s^2\left(\sqrt{g}\right)^{2/3}\left[\alpha\left|\hat{\overline{S}}\right|\widehat{\overline{S_{ij}}} - \widehat{\left|\overline{S}\right|\overline{S_{ij}}}\right] \\ &= -2C_s^2\left(\sqrt{g}\right)^{2/3}M_{ij}\end{aligned} \tag{8}$$

Here α is the square of the ratio of the characteristic length scale associated with the test filter to that of grid filter and is taken to be $\left[\widehat{\overline{\Delta}}_i / \overline{\Delta}_i = \sqrt{6}\right]$ for a representative one-dimensional test filtering operation. Using a least-squares minimization procedure of Lilly [47], a final expression for $C_s^{\,2}$ is obtained as:

$$C_s^{\,2} = -\frac{1}{2}\frac{1}{(\sqrt{g})^{2/3}}\frac{L_{ij}^a \bullet M_{ij}}{M_{ij} \bullet M_{ij}} \tag{9}$$

The value of $C_s^{\,2}$ is constrained to be positive by setting it to zero when $C_s^{\,2} < 0$. The mean non-dimensional pressure gradient β is assumed to be unity in Equation (3), whereas γ is calculated from a global energy balance as: $\gamma = \frac{q_w^{''}\Omega}{Re_\tau Pr Q_x L_x}$ in Equation (4).

2.2 Zonal two layer flow model

The zonal two layer model formulation implemented in the generalized coordinate system (ξ, η, ζ) is described in this section briefly in a very simplified form.

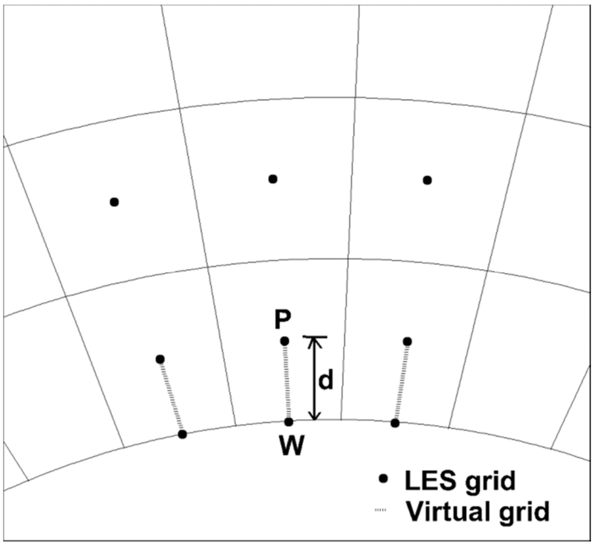

Figure 1: Virtual grid for wall model, embedded in LES grid (W represent wall node. P represent first off wall LES grid node)

Figure 1 shows the virtual grid in the wall normal direction required for the two layer wall model embedded in the outer LES grid. Simplified turbulent boundary layer equations of form described by Equation (1) are solved on this virtual grid. Instead of using (*x,y,z*) or (ξ, η, ζ) coordinate systems, a coordinate system of reduced dimensionality *(t,n)* is used where *t* is the tangential and *n* is the normal direction to the wall. Neglecting the unsteady and convection terms on the LHS of Equation (1), it can be written as

$$\frac{\partial}{\partial n}\left[\left(\frac{1}{\text{Re}}+\frac{1}{\text{Re}_t}\right)\frac{\partial u_t}{\partial n}\right]=\frac{\partial P}{\partial t} \tag{10}$$

The Cartesian components of the velocity vector at the first nodal point off the wall are used to find the tangential velocity (U_t), which serves as the boundary condition for the inner layer. Similarly, the pressure gradient in the tangential velocity direction $(\partial P/\partial t)$ is also calculated using the outer LES and is assumed constant in the inner layer. Equation (10) is solved on an embedded virtual grid in the wall normal direction with a no-slip boundary condition at the wall. The turbulent viscosity ν_t is modeled based on mixing length theory with near-wall damping.

$$\frac{1}{\text{Re}_t}=\frac{\kappa}{\text{Re}}d^+\left(1-e^{-d^+/A}\right)^2 \tag{11}$$

Where, κ is Von-Karman constant, d is normal distance from the wall, A= 19 and,

$$d^+=\frac{u_\tau d}{\nu} \tag{12}$$

$$u_\tau=\sqrt{\frac{\tau_w}{\rho}} \tag{13}$$

$$\|\tau_w\|=\left(\frac{1}{\text{Re}}+\frac{1}{\text{Re}_t}\right)\frac{\partial u_t}{\partial n}\Big|_{wall} \tag{14}$$

Equation (10) is discretized using the second order central difference scheme and solved using an efficient tri-diagonal solver. Equation (14) is then used to obtain the wall shear stress in the tangential direction, the components of which are then transformed back into a (*x,y,z*) coordinate system to act as boundary conditions in the respective momentum equations for the outer flow completing the coupling with the outer flow.

2.3 Zonal two layer heat transfer model

The energy equation for turbulent flows in conservative non-dimensional form for a coordinate system of reduced dimensionality *(t,n)* with absence of additional source terms can be written as

$$\frac{\partial}{\partial n}\left[\left(1+\frac{\text{Re}\cdot\text{Pr}}{\text{Re}_t\cdot\text{Pr}_t}\right)\frac{\partial\theta}{\partial n}\right]=0 \tag{15}$$

The solution of Equation (15) requires the closure model for the turbulent Prandtl number. For the current investigation, the formulation of Kays [48] is used and presented in Equation (16).

$$1/\text{Pr}_t=0.58+0.22\left(\frac{\text{Re}}{\text{Re}_t}\right)-0.0441\left(\frac{\text{Re}}{\text{Re}_t}\right)^2\left\{1-\exp\left[\frac{-5.165}{\left(\frac{\text{Re}}{\text{Re}_t}\right)}\right]\right\} \tag{16}$$

This formulation accounts for the higher values of turbulent Prandtl number very close to the wall and its gradual decay away from the wall. Experimental as well as numerical simulations of wall bounded turbulent flows have shown [48] that values of turbulent Prandtl number are higher near wall (y^+<15) as against to approximately constant value away from the wall. Equation (15) is solved in the inner layer zonal mesh in a same way as Equation (10). The temperature at the first LES grid point off the wall and either the specified wall temperature or the surface heat flux are used as boundary conditions for solving Equation (15).

If the heat flux at the wall is specified, then there is no change in the energy equation calculation for the outer layer. Still, Equation (15) is solved in the inner layer to obtain the wall temperature using the outer LES temperature and specified wall heat flux as a boundary condition. The temperature profile obtained from solving Equation (15) in the inner layer is used to calculate the wall temperature as follows

$$\theta_{wall} = \theta_{i2} + \frac{\Delta d}{\left(1 + \frac{\mathrm{Re}\,\mathrm{Pr}}{\mathrm{Re}_t\,\mathrm{Pr}_t}\right)} \tag{17}$$

Where, θ_{i2} is the temperature at the first off wall inner layer nodal point and Δd is its normal distance from the wall.

2.4 Numerical method

The governing equations for momentum and energy are discretized with a conservative finite-volume formulation using a second-order central difference scheme on a non-staggered grid topology. The Cartesian velocities, pressure, and temperature are calculated and stored at the cell center, whereas contravariant fluxes are stored and calculated at cell faces. For the time integration of the discretized continuity and momentum equations, a projection method is used. The temporal advancement is performed in two steps, a predictor step, which calculates an intermediate velocity field, and a corrector step, which calculates the updated velocity at the new time step by satisfying discrete continuity. The energy equation is advanced in time by the predictor step. The computer program Generalized Incompressible Direct and Large Eddy Simulations of Turbulence (GenIDLEST) used for current study has been applied and validated for numerous complex heat transfer and fluid flow problems. Details about the algorithm, functionality, and capabilities can be found in Tafti [49, 50]

All calculations were performed on 4 Apple Xserve G5 compute nodes with 2.3 GHz PowerPC 970FX processor. For integrating over one non-dimensional time unit (with a time step of 5×10^{-4}), about two hours of wall clock time is required for case 1 in Table 2, while about one hour of wall clock time is required for case 2 and case 3. Inner layer calculations for 32 virtual nodes require less than 10% of the outer LES calculation time.

3 RESULTS

3.1 Computational domain

Figure 2 describes the computational domain for two different Reynolds number used for current investigation. Geometries investigated for both Reynolds numbers had a square cross section and ribs normal to the flow direction. Ratio of rib height to the duct hydraulic diameter (e/D_h) was 0.1 and 0.05 while ratio of rib pitch to height was 10 and 20 for Reynolds number of 20,000 and 60,000 respectively. The computational methodology discussed in section 2 assumes the flow and heat transfer to be fully developed. Hence the computational domain length in streamwise (x) direction is taken to be a periodic segment between two adjacent ribs in the experimental geometry of Rau et al. [1] and Han et al. [2]. In this framework, a mean pressure driving force is applied to the domain and the flow develops to reach a stationary state when the mean losses in the domain are balanced by the applied mean pressure gradient.

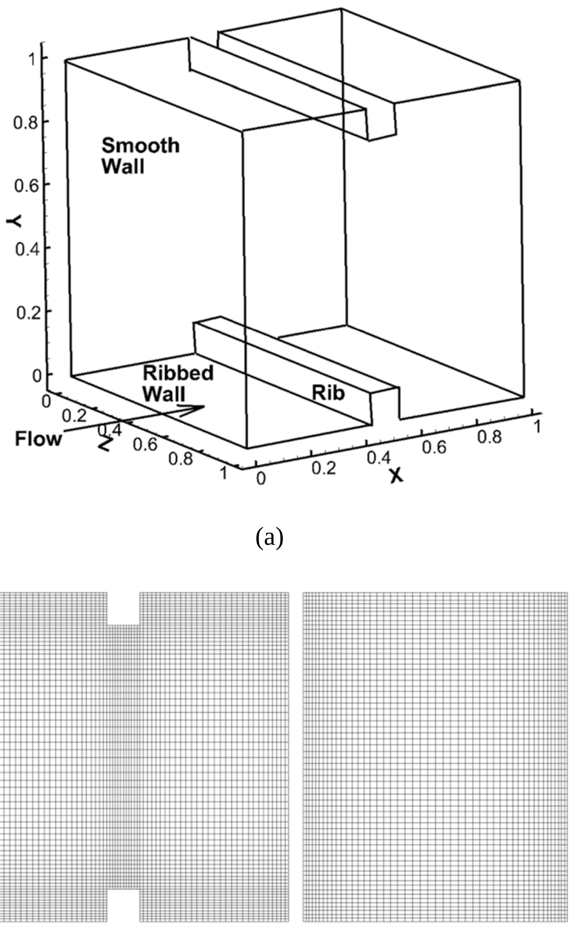

Figure 2: (a) Computational domain, and mesh at (b) z=0.5 section (c) x=0.5 section; for ribbed duct calculations

3.2 Validation of heat transfer wall model in a turbulent channel flow

Table 1 summarizes the calculations performed in a fully developed turbulent channel flow to validate the heat transfer wall model used in conjunction with the velocity wall model.

Table 1: Turbulent channel flow calculation summary

	Re_τ	Δ_x^+	Y^+	Δ_z^+	Nu	Nu_0	f	f_c
LES	590	19	0.8	9	106	105.4	0.022	0.0215
WMLES	590	60	30	30	108.5	105.4	0.021	0.0215
WMLES (only for flow)	590	60	30	30	70	105.4	0.021	0.0215

Well resolved LES is performed for a Reynolds number (Re_τ) of 590 based on the shear velocity and the channel half height. Flow data from DNS calculations of Moser et al. [51] is used to validate the wall resolved LES calculations. A summary of the grid resolution is presented in Table 1. A very fine grid with Y^+ =0.8, Δx^+=19, and Δz^+=9 was used for the wall resolved LES in a computational domain of size $2\pi\delta \times 2\delta \times \pi\delta$ in x, y, and z direction respectively, where δ is the half channel height. Total grid cells of 7.5 million were used with 196 grid points in x (streamwise) and z (spanwise), and y (wall normal) direction. The dynamic Smagorinsky model was used to include the effects of subgrid scales. The wall resolved LES calculation used a no slip boundary conditions at the channel walls for flow variables and constant heat flux boundary condition for temperature. Periodic conditions were applied in the streamwise and spanwise direction. Figure 3 compares results of LES with the DNS data of Moser et al. [51]. It is clear that the mean flow velocity profile matches in exact agreement with the DNS data. Also, all the Reynolds stresses match in very close agreement with the DNS data. This indicates that the grid resolution used for the LES calculation was sufficient to be considered as well resolved LES calculation. The heat transfer data from this resolved LES was further used for validating the results from the wall model.

A coarse mesh was constructed for wall modeled LES calculations with Y^+ =30, Δx^+=60, and Δz^+=60 in the same computational domain. The zonal near wall treatment for velocity as well as temperature, discussed in section 2, was used for these wall modeled LES (WMLES) calculations. From Figure 3 it can be seen that the WMLES calculations were able to predict the mean flow velocity and temperature profiles in close agreement with LES predictions. The detailed validation of flow variables has been carried out by Patil and Tafti [52]. Friction factor calculated by WMLES matches well with the one obtained by wall resolved LES and an experimental correlation value (f_c) [53].

$$f_c = 0.184 \times \mathrm{Re}_{D_h}^{-1/5} \quad (18)$$

It is important to note that the time averaged Nusselt number values predicted by LES and WMLES calculations match closely at 106 and 108.5, respectively, which also match well with the value of 105.4 obtained from the Dittus-Boelter correlation (Nu_0) [54].

$$Nu_0 = 0.023 \times \mathrm{Re}^{0.8} \times \mathrm{Pr}^{0.4} \quad (19)$$

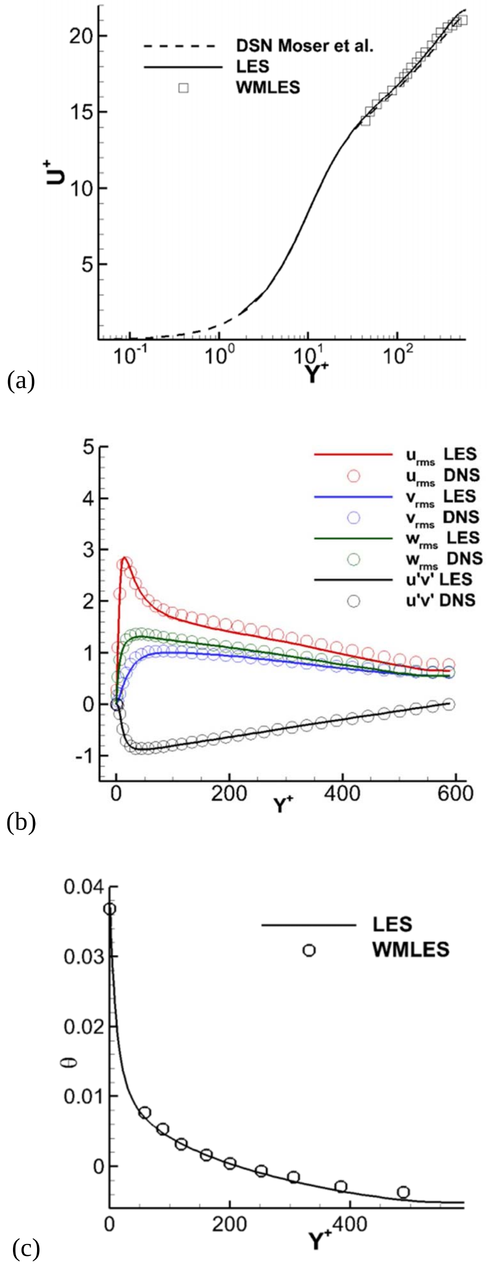

Figure 3 Validation of heat transfer wall model in a turbulent channel flow (a) mean velocity profile (b) Variation of rms turbulent Reynolds stresses (c) mean temperature profile

Furthermore, a calculation was performed with the zonal treatment for velocity only to quantify the benefits of the heat transfer wall model. With this calculation, the Nusselt number was under predicted by about 25% compared to LES and the Dittus-Boelter correlation. This observation leads to a conclusion that even though the velocity predictions are accurate with the zonal treatment of the momentum equations, solving the energy equation without a wall model on a coarse near wall mesh results in large under prediction of the surface heat transfer coefficient. It is also noteworthy to mention that LES calculations without zonal velocity as well as heat transfer model on the coarse mesh results in more than 25% underprediction of skin friction and Nusselt number.

Comparing the spatio-temporal resolution for wall resolved LES versus the wall modeled LES, the computational complexity was reduced by a factor of 285 by using the wall modeled LES.

3.3 Ribbed Duct

Table 2 summarizes the calculations performed on the ribbed duct geometry.

Table 2: Ribbed duct calculation summary

Case	Re_τ	Re_b	grid resolution	Y^+	near wall treatment
1	6667	20000	72×72×64	15-30	Zonal
2	6667	20000	56×56×48	20-30	Zonal
3	6667	22200	56×56×48	20-30	none
4	12533	60000	88×88×88	20-40	Zonal

Two different Reynolds numbers were investigated with wall modeled LES and LES without wall model. The Reynolds number is based on the duct hydraulic diameter and the bulk mean velocity inside it. A grid sensitivity study is reported for the Reynolds number of 20,000. All the grids were designed to perform the wall modeled LES calculations; but a calculation without wall model was performed on the same grid to evaluate the benefit of using the wall model in predicting the skin friction and surface heat transfer coefficient on a coarse mesh. LES calculations with the zonal near wall model on grids 1 and 2 resulted in overall predictions without any significant difference. Further coarsening of grid 2 uniformly in all directions (not shown) resulted in Nusselt numbers predictions significantly different from experimental values.

Table 3 summarizes the results for Reynolds number of 20,000 for different grids. Grids for case 1 and 2 resulted in similar overall predictions. It is clear from Table 3 that the zonal two-layer formulation presented in section 2 for the heat transfer is able to predict the surface heat transfer coefficient in very close agreement with the experimental data and wall resolved LES calculations of Tafti [3]. The predictions of the skin friction is also in close agreement with data and wall resolved LES calculation of Tafti [3] indicating that the zonal two-layer formulation presented in section 2 works well in predicting the near wall region. The benefit of using wall model becomes evident in case 3 in which LES calculations without a wall model are performed on a coarse mesh. This results in large under predictions of skin friction and surface heat transfer coefficient.

Comparing the spatial resolution (128^3) for wall resolved LES of Tafti [3] and a time step of 5×10^{-5}, Case 1 in Table 2, reduces the computational complexity by a factor of 63, whereas Case 2 and 3 reduce the complexity of the computation by a factor of 140.

Table 3: Heat transfer and friction data comparison with Rau et al. [1] (Re=20,000)

	LES calculations, $\frac{e}{D_h}=0.1, \frac{p}{e}=10$				Experiment
	case1	case 2	case 3	Tafti [3]	Rau et al. [1]
Re_τ	6667	6667	6667	6667	-
Re_b	20,000	20,000	22,200	20,000	30,000
% form loss	90	90	95	91	85
Reattachment length (x_r/e)	4.2	4.2	4.5	4.1	4.0-4.25
$\langle Nu\rangle/Nu_0$ ($Nu_0=0.023.Re_b^{0.8}.Pr^{0.4}$)					
Rib	2.49	2.46	1.96	2.89	-
Ribbed Wall	2.20(7.9%)	2.21 (7.9%)	1.82 (24%)	2.4	2.40
Smooth Wall	1.91 (6 %)	1.92 (6%)	1.48 (28%)	1.89	2.05
Overall with rib	2.13	2.14	1.76	2.23	-
Overall w/o rib	2.05 (6%)	2.06 (6.9 %)	1.69 (23%)	2.14	2.21
f/f_0 ($f_0=0.046\,.Re_b^{-0.2}$)					
Overall	8.5 (10%)	8.5 (10%)	7.25 (24%)	8.6	9.5

Experimental uncertainty is ±5%

3.4 Ribbed duct flow at Re_{Dh} = 20,000

All the calculations for the bulk Reynolds number of 20,000 were performed at $Re_\tau = 6667$ with a mean pressure gradient of unity applied in the flow direction. The non-dimensional time step in these calculations was set to 5×10^{-4}which is an order of magnitude higher than the one used by Tafti [3] for his wall resolved calculation on the same geometry and Reynolds number with 128 grid nodes in all directions. The viscous terms are treated implicitly. The average L_1 residual norm of global mass balance is converged to 1×10^{-8}, while the momentum and energy equations in the implicit treatment are converged to 1×10^{-7}. Calculations were initialized assuming an initial mass flow rate and integrated in time until the flow rate adjusts to the balance between internal losses and specified mean pressure gradient. After this point when the flow rate reaches an asymptotic value, data sampling was initiated to extract the mean flow and turbulent statistics. The total sampling interval was 10 non-dimensional time units. The local Nusselt number is calculated as

$$Nu = \frac{1}{\theta_s - \theta_{ref}} \tag{20}$$

where θ_s is the surface temperature and θ_{ref} is the reference temperature defined as

$$\theta_{ref} = \frac{\iint |u_1|\theta dA_x}{\iint |u_1| dA_x} \tag{21}$$

The surface-averaged Nusselt number is obtained by averaging the local Nusselt number as

$$\langle Nu \rangle = \frac{1}{\iint\limits_{\Omega} ds} \left[\iint\limits_{\Omega} \frac{1}{\theta_s - \theta_{ref}} ds \right] \qquad (22)$$

where s denotes the surface under consideration. Based on the non-dimensional mean pressure gradient of unity, the Fanning friction factor is calculated as

$$f = \frac{1}{2.\overline{u_b}^2} \qquad (23)$$

Figure 4(a) shows the mean streamline pattern at the center of the duct ($z = 0.5$) for case 1. All three cases for bulk Reynolds number of 20,000 showed presence of the leading edge vortex at the rib-wall junction, the counter-rotating vortex in the wake region of the rib and the recirculation region downstream of the rib. For case 1 and case 2 the reattachment length is found to be 4.1 rib heights downstream of the rib, which is in exact agreement with the wall resolved calculation of Tafti [3]. Rau et al. [1] also reported this value to be in the range of 4.0 to 4.3 rib heights.

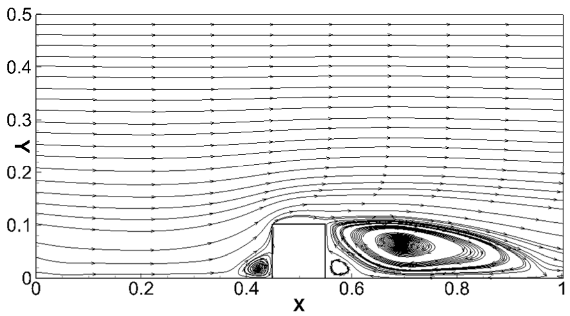

(a)

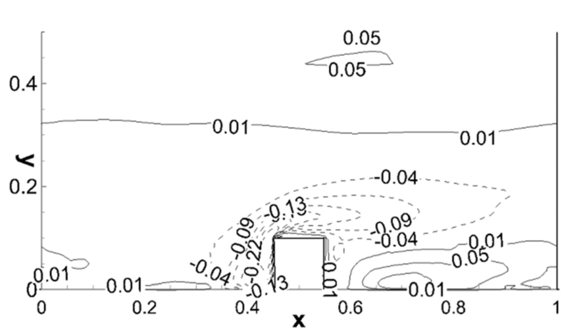

(b)

Figure 4: (a)Mean streamline distribution in the z-symmetry ($z = 0.5$) plane (b) Contours of mean spanwise flow velocity near smooth wall ($z = 0.07$) at Re=20,000

Figure 4(b) represents the spanwise velocity distribution in the vicinity of the side smooth wall for case 1. The flow predicted has three dimensional behavior near the smooth wall with mean spanwise (w_b) velocity reaching up to 22% of the mean streamwise velocity ($\overline{u_b}$). The localized phenomenon of strong spanwise velocity moving towards and impinging on the smooth wall within the confines of the shear layer at the leading edge of the rib is a result of unsteady vorticity which is produced and transported at the junction of the rib with the smooth wall. This phenomenon is captured well with the WMLES calculation, but is missed by most eddy-viscosity RANS models.

Figure 5 shows contours of time averaged Reynolds normal stresses (u_{rms}, v_{rms}, w_{rms}) and Reynolds shear stress ($\overline{u'v'}$) at the center plane of the duct ($z = 0.5$). Reynolds normal stresses are normalized by the bulk mean velocity while the Reynolds shear stresses are normalized by the square of the bulk mean velocity in the duct. The time averaged variance of the streamwise velocity (u_{rms}) in figure 5(a) takes a maximum value in the separated shear layer at the leading edge of the rib, with values between 40% and 50%. They are lowest in the stagnating flow at the rib and in the recirculation immediately behind the rib as observed by Tafti [3]. Figure 5(e) represents the distribution of the variance of streamwise velocity (u_{rms}) in the region between the two ribs ($\frac{x'}{e} = 4.5$). This location is in the recovery region downstream of the reattachment point. The maximum values of u_{rms} in the shear layer behind the ribs and at the duct center ($y = 0.5$) were predicted to be around 38% and 15% respectively, which are in close agreement with the experimental values of 35% and 14%, respectively, in the shear layer and center, reported by Rau et al. [2]. The time averaged variance of transverse velocity (v_{rms}) at the center plane of the duct ($z = 0.5$) is plotted in figure 5(b). The maximum value of v_{rms} in the separated shear layer downstream of the rib and at the center of the duct ($y = 0.5$) are predicted to be 22% and 12% respectively. These values compare in exact agreement with the experimental values of Rau et al. [1].

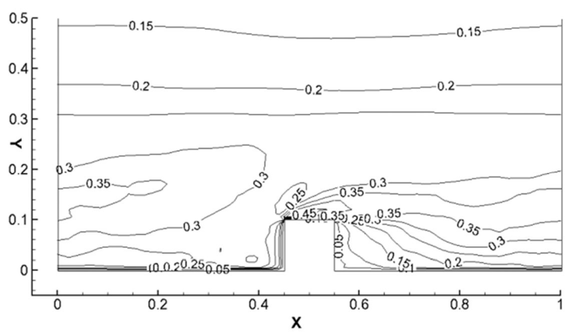

(a) u_{rms}

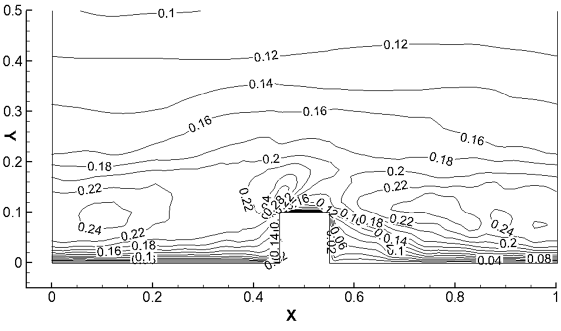

(b) v_{rms}

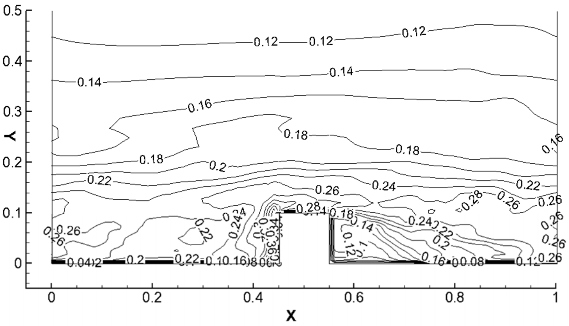

(c)w_{rms}

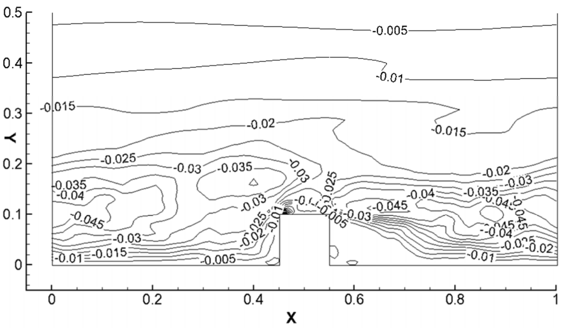

(d) $u'v'$

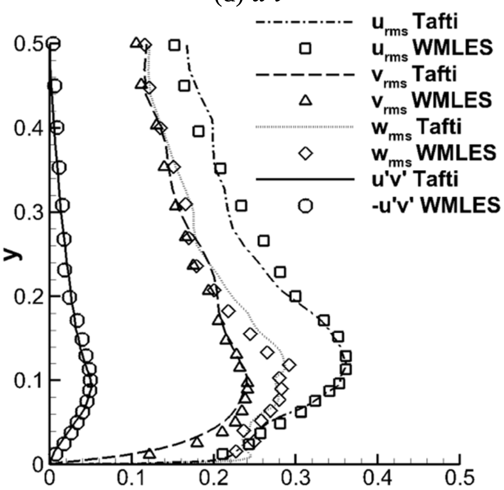

(e) RMS turbulence statistics

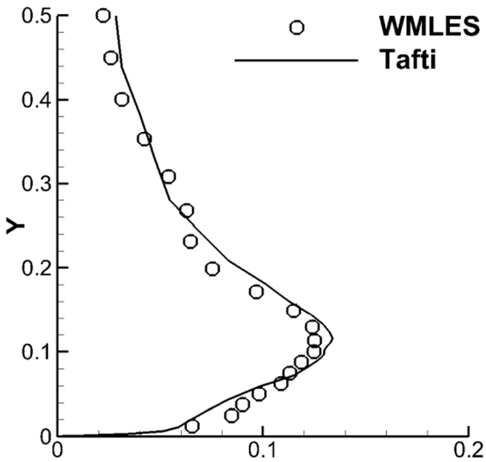

(f) Turbulent kinetic energy

Figure 5: Distribution of Reynolds normal stresses and shear stress at center plane ($z = 0.5$), and variation of RMS turbulence quantities at center plane ($z = 0.5, x = 1$) (Re=20,000)

Figure 5(c) present the time averaged variance of spanwise velocity (w_{rms}) at the center plane of the duct ($z = 0.5$). w_{rms} shows a maximum value of about 36% at the top leading edge of the rib. High spanwise intensities are observed because of the impingement of eddies at the leading edge of the rib. This phenomenon is further explained in detail by Tafti [3]. The spanwise fluctuation are also high in the shear layer downstream of the rib with a maximum value of about 30% as shown in figure 5(e).

Figure 5(d) shows the distribution of the time averaged Reynolds shear stress ($\overline{u'v'}$) in the center plane of duct ($z = 0.5$). Distribution of -$\overline{u'v'}$ is shown in figure 5(e) in the wall normal direction. The Reynolds shear stress reaches a maximum value of about -4.5% in the separated shear layer downstream of the rib.

The turbulent kinetic energy was observed to be maximum near the origin of the shear layer on the rib and decays to lower values as the flow reaches the next rib. The values near the ribbed wall are between 6% and 8% throughout the length of the channel, except the recirculation region behind the rib. Figure 5(f) represent the distribution of turbulent kinetic energy at the center plane ($z = 0.5$, x=1). The maximum value (14%) of tke in the shear layer is predicted well as compared to LES of Tafti [3].

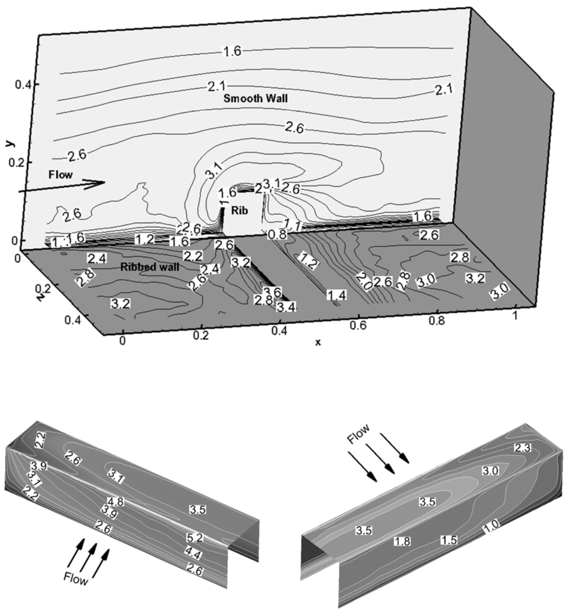

Figure 6: Contours of Nusselt number on (a)smooth wall and ribbed wall, and (b) ribs (only half of the rib is shown) (Re=20,000)

Figure 6 shows Nusselt augmentation distribution (with respect to the Dittus-Boelter correlation for a smooth duct) for the WMLES calculation. Heat transfer augmentation is low in the recirculation region immediately downstream of the rib but increases further downstream to reach a maximum near the reattachment region. The augmentation decreases as the smooth wall is approached with values close to unity at the corners. On the smooth wall, higher heat transfer augmentation occurs in the vicinity of the rib junction. This is a result of lateral flow impingement on the wall as shown in figure 4. Maximum heat transfer occurs on the leading edge of the ribs with values as high as 6. This can be attributed to strong flow acceleration in this region.

Figure 7 compares the predicted heat transfer augmentation by WMLES calculations with the experimental data of Rau et al. [1] at the center of the ribbed wall ($z = 0.5$) and at a location $0.5e$ upstream of the rib along the smooth wall. The predictions are in close agreement with the experimental data. The results show that WMLES not only predicts the surface averaged heat transfer coefficients with accuracy but also the local distributions consistent with the LES study of Tafti [3], unlike RANS based modeling which in many instances gives reasonable surface averaged heat transfer coefficients but with substantially different local distribution.

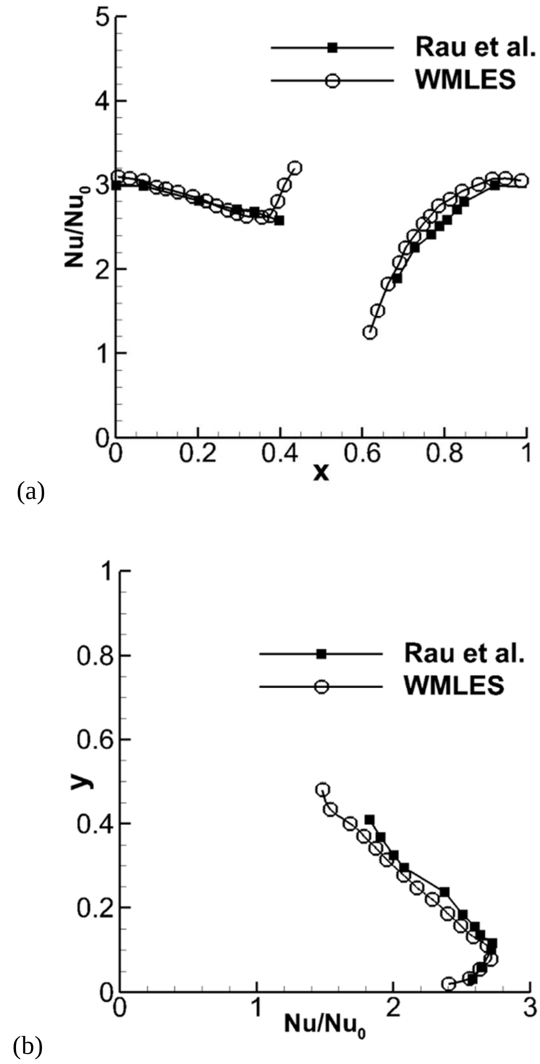

Figure 7: Comparison of Nusselt augmentation with experimental data of Rau at al. [1] at (a) ribbed wall at center plane, $y = 0, z = 0.5$ (b)smooth wall at $e/2$ upstream of rib, $z = 0, x = 0.4$ (Re=20,000)

3.5 Ribbed duct flow at Re_{Dh} 60,000

Calculations for the bulk Reynolds number of 60,000 were performed with ratio of rib height to the hydraulic diameter of the duct (e/D_h) 0.05 and ratio of rib pitch to height of 20. The computational methodology described for Re=20,000 was applied for this case. A grid of 81×81×81 was used in the computational domain with Y^+ values in the range of 25-50. Predictions with WMLES calculations are compared with limited experimental data of Han et al. [2]. Experimental data for flow measurements is not provided. The measured distribution of Nusselt number on the ribbed wall along the centerline ($z = 0.5$) is reported.

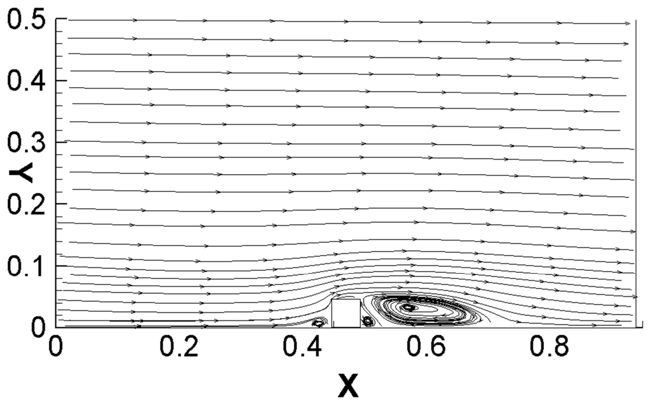

Figure 8: Mean streamline distribution in the z-symmetry ($z = 0.5$) plane (Re=60,000)

Figure 8 represents the mean streamline structure at the center plane ($z = 0.5$) of the duct. The major flow structures are similar to that at Re=20,000. The reattachment length is found to be about three times the rib height. Figure 9(a) and 9(b) represent the turbulent intensities and the mean turbulent kinetic energy variation along the duct height.

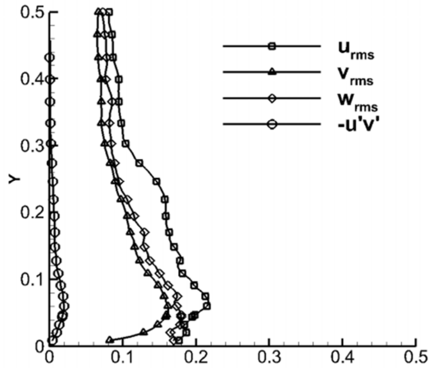

(a)

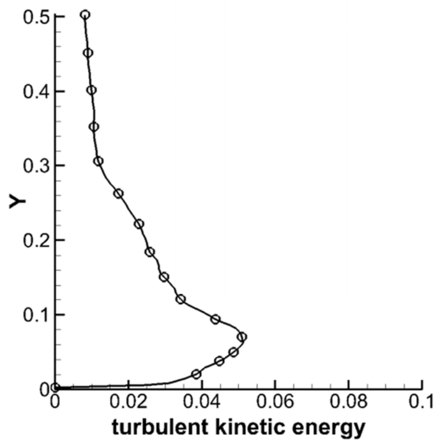

(b)

Figure 9: Reynolds stresses and at center plane ($z = 0.5, \frac{x'}{e} = 8.5$) (Re=60,000)

Comparing the values with the Re=20,000 case, it can be observed that the values of these turbulence quantities are significantly lower. This indicates that the configuration at Re=60,000 with a smaller ratio of rib height to the hydraulic diameter of the duct and higher ratio of pitch to height results in less turbulence production compared with the Re=20,000 case.

Figure 10 compares the predictions of Nusselt augmentation ratio at the center line of duct ($z = 0.5$) on the ribbed wall. WMLES captures the trends in the heat transfer augmentation as well as the values of Nusselt augmentation in close agreement with the experimental data of Han et al. [2]. The trends in surface heat transfer coefficient distribution on the ribbed and smooth walls are similar to the one observed for Re=20,000 case. The maximum value of the Nusselt augmentation occurs at the leading edge of the rib facing the flow. Highly energetic unsteady eddies upstream of the rib are responsible for the flow acceleration and hence the higher magnitudes of the heat transfer augmentation. In the region immediately downstream of the rib, the flow is weak resulting in very low values of the heat transfer augmentation approaching unity. The Nusselt augmentation values slowly increases and reaches higher magnitudes near the flow reattachment length. These values remain high in the attached region following the reattachment point. It is noteworthy to mention that the difference in predictions and the measurements is small and within experimental uncertainty.

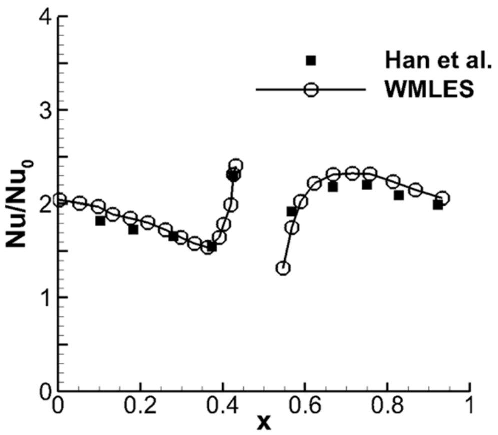

Figure 10: Comparison of Nusselt augmentation with experimental data of Han at al. [40] at center plane ($z = 0.5, y = 0$) (Re=60,000)

Han et al. [2] also reported values heat transfer augmentation distribution on the centerline (y= 0.5) of smooth wall along the length of the duct. They reported these values in a very small range of 1.35 to 1.45. Predictions from the WMLES calculation also agree with this observation with a value in the range 1.4 to 1.55. Average value of Nusselt augmentation on smooth wall predicted by WMLES is 1.5 which is slightly higher than the value of 1.4 reported by Han et al. [2]. Average value of Nusselt augmentation on the ribbed wall was predicted to be 2.15 by WMLES. This value is slightly over predicted than the reported value of 2.0 by Han et al. [2]. These average values of heat transfer augmentation are lower compared with Re=20,000 case owing to lower turbulence intensities. The overall friction factor augmentation was predicted to be 4.1 by WMLES, which matches in exact agreement with the value reported by Han et al. [2]. The base friction factor (f_{FD}) was calculated by using Blausius equation (Equation 24) for the four-sided smooth channel.

$$f_{FD} = 0.079 \times \mathrm{Re}^{-0.25} \qquad (24)$$

4. CONCLUSIONS

LES calculations are performed in a square duct with different ratios of rib height to hydraulic diameter of duct and rib height to pitch for Reynolds number of 20,000 and 60,000. All calculations use the dynamic Smagorinsky subgrid scale model with a second-order central difference scheme. The zonal near wall treatment is used for flow variables as well as temperature. Mean flow, turbulence, and heat transfer predictions from WMLES calculations are compared with experimental data of Rau et al. [1], Han et al. [2] and well resolved LES data of Tafti [3].

WMLES calculations predict the friction factor and Nusselt augmentation in close agreement with the experimental data for both Reynolds numbers investigated. The major flow features like unsteady energetic eddies near the rib wall, recirculation zone behind the rib, corner eddy, reattachment location, are in close agreement with experimental observations and well resolves LES predictions. Trends in the surface heat transfer coefficient distribution as well as values of Nusselt augmentation were predicted well within the experimental uncertainty for both the Reynolds numbers.

To quantify the advantage of using wall models, LES calculations without a zonal near wall treatment were performed on a coarse mesh designed for WMLES. It was observed that these LES calculations without any wall model under predict the friction factor and Nusselt augmentation significantly on a coarse near wall mesh. The advantage of using a wall model both for flow and heat transfer becomes more pronounced at higher Reynolds numbers. It is noteworthy to mention that the timestep required for the current calculations are order of magnitude higher than the time step required for a wall resolved LES. The computational time required by WMLES are 60-140 times lower than that required for wall resolved LES calculations for the calculations in this paper.

NOMENCLATURE

C_p	specific heat
D_h	hydraulic diameter
e	rib height
f	Fanning friction factor
k	thermal conductivity
L_x	domain length in streamwise (x) direction
$\vec{n}$	surface normal vector
Nu	Nusselt number
P	Rib pitch or total pressure
p	fluctuating pressure
Pr	Prandtl number
Pr_t	Turbulent Prandtl number
q_w''	wall heat flux
Q_x	flow rate in x direction
Re_b	Reynolds number based on bulk velocity($=\frac{\bar{u}_b D_h}{\nu}$)
Re_τ	Reynolds number based on shear velocity($=\frac{u_\tau D_h}{\nu}$)
Re_t	inverse of turbulent (eddy) viscosity
T	temperature
$\vec{u}$	Cartesian velocity vector
u_τ	friction velocity
x'	distance from downstream of the rib
β	mean pressure gradient
γ	mean temperature gradient
θ	non-dimensional temperature
Ω	total heat transfer surface area

Subscripts

S	surface
b	bulk mean time averaged velocity
0	smooth duct
rms	root mean square
c	correlation

ACKNOWLEDGMENTS

The calculations were performed on Virginia Tech's Terascale computing facility, System-X. The support is gratefully acknowledged. We also acknowledge the support provided by Solar Turbines in gas turbine combustor liner heat transfer, which motivated the authors in doing this study.

REFERENCES

[1] Rau G., Cakan M., Moeller D., and Arts T., 1998. "The Effect of periodic ribs on the local aerodynamic and heat transfer performance of a straight cooling channel. ASME Journal of Turbomachinery, **120**, 368–375.

[2] Han J. C., Park J. S., and Ibrahim M. Y., 1986. "Mesurement of heat transfer and pressure drop in rectangular channels with turbulence promoters," NASA report 4015.

[3] Tafti D. K., 2004. "Evaluating the role of subgrid stress modeling in a ribbed duct for the internal cooling of turbine blades," International Journal of Heat and Fluid Flow, **26**, 92–104.

[4] Han J. C., 1984. "Heat transfer and friction in channels with two opposite rib-roughened walls." ASME Journal of Heat Transfer, **106**, 774–781.

[5] Han J. C., 1988. "Heat transfer and friction characteristics in rectangular channels with rib turbulators," ASME Journal of Heat Transfer, **110**, 321–328.
[6] Chandra P. R., Han J. C., and Lau S. C., 1988. "Effect of rib angle on local heat/mass transfer distribution in a two-pass rib-roughened channel," ASME Journal of Turbomachinery, **110**, 233–241.
[7] Lau S. C., McMillan R. D., and Han J. C., 1991a. "Turbulent heat transfer and friction in a square channel with discrete rib turbulators," ASME Journal of Turbomachinery, **113**, 360–366.
[8] Han J. C., and Zhang Y. M., 1991. "Effect of rib-angle orientation on local mass transfer distribution in a three-pass rib-roughened channel," ASME Journal of Turbomachinery, **113**, 123–130.
[9] Han J. C., Zhang Y. M., and Lee C. P., 1992. "Influence of surface heat flux ratio on heat transfer augmentation in square channels with parallel, crossed, and V-shaped angled ribs," ASME Journal of Turbomachinery, **114**, 872–880.
[10] Han J. C., Al-Qahtani M., and Chen H. C., 2002. "A numerical study of flow and heat transfer in rotating rectangular channels with 45^o rib turbulators by Reynolds stress turbulence model," In: Proceedings of the ASME Turbo Expo 2002, GT-2002-30216.
[11] Ekkad S. V., and Han J. C., 1997. "Detailed heat transfer distributions in two-pass square channels with rib turbulators," International Journal of Heat Mass Transfer, **40(11)**, 2525–2537.
[12] Taslim M. E., Li T., and Spring S. D., 1998. "Measurements of heat transfer coefficients and friction factors in passages rib-roughened on all walls," ASME Journal of Turbomachinery, **120**, 564–570.
[13] Korotky G. J., and Taslim M. E., 1998. "Rib heat transfer coefficient measurements in a rib-roughened square passage," ASME Journal of Turbomachinery, **120**, 376–385.
[14] Taslim M. E., and Lengkong, 1998. "45 degree staggered rib heat transfer coefficient measurements in a square channel," ASME Journal of Turbomachinery, **120**, 571–580.
[15] Taslim M. E., and Korotky G. J., 1998. "Low-aspect ratio rib heat transfer coefficient measurements in a square channel.," ASME Journal of Turbomachinery, **120**, 831–838.
[16] Saidi A., and Sunden B., 2001. "On prediction of thermal-hydraulic characteristics of square-sectioned ribbed cooling ducts," ASME Journal of Turbomachinery, **123**, 614–620.
[17] Jia R., Saidi A., and Sunden B., 2002. "Heat transfer enhancement in square ducts with V-shaped ribs of various angles," In: Proceedings of the ASME Turbo Expo 2002, Amsterdam, The Netherlands, ASME Paper No. GT-2002-30209.
[18] Iacovides H., Kelemenis G., and Raisee M., 2003. "Flow and heat transfer in straight cooling passages with inclined ribs on opposite walls: an experimental and computational study," Experimental Thermal and Fluid Science, **27**, 283–294.
[19] Ooi A., Iaccarino G., Durbin P. A., and Behnia M., 2002. "Reynolds averaged simulation of flow and heat transfer in ribbed ducts," International Journal of Heat and Fluid Flow, **23**, 750–757.
[20] Prakash C., and Zerkle R., 1995. "Prediction of turbulent flow and heat transfer in a ribbed rectangular duct with and without rotation," ASME Journal of Turbomachinery, **117**, 255–264.
[21] Jang Y.-J., Chen H.-C., and Han, J.-C., 2001. "Flow and heat transfer in a rotating square channel with 45 deg angled ribs by Reynolds stress turbulence model," ASME Journal of Turbomachinery, **123**, 124–132.
[22] Chen Y., Nikitopoulos D. E., Hibbs R., Acharya S., and Myrum T. A., 2000. "Detailed mass transfer distribution in a ribbed coolant passage with a 180^0 bend," International Journal of Heat and Mass Transfer, **43**, 1479–1492.
[23] Iacovides H., 1998. "Computation of flow and heat transfer through rotating ribbed passages," International Journal of Heat and Fluid Flow, **19**, 393–400.
[24] Han J. C., Chandra P. R., and Lau S. C., 1988. "Local heat/mass transfer distributions around sharp 180 deg turns in two-pass smooth and ribroughened channels," ASME Journal of Heat Transfer, **110**, 91–98.
[25] Murata A., and Mochizuki S., 2001. "Comparison between laminar and turbulent heat transfer in a stationary square duct with transverse or angled rib turbulators," International Journal of Heat and Mass Transfer, **44**, 1127–1141.
[26] Abdel-Wahab S., and Tafti D. K., 2004a. "Large eddy simulation of flow and heat transfer in a 90^0 ribbed duct with rotation: effect of Coriolis and centrifugal buoyancy forces," ASME Journal of Turbomachinery, **126**, 627–636.
[27] Abdel-Wahab S., and Tafti D. K., 2004b. "Large eddy simulation of flow and heat transfer in a staggered 45^0 ribbed duct," In: Proceedings of the ASME Turbo Expo 2004, Vienna, Austria, ASME Paper No. GT2004-53800.
[28] Sewall E. A., and Tafti D.K., 2004a. "Large eddy simulation of the developing region of a stationary ribbed internal turbine blade cooling channel," In: Proceedings of the ASME Turbo Expo 2004, Vienna, Austria, ASME Paper No. GT2004-53832.
[29] Chapman D. R., 1979. "Computational aerodynamics, development and outlook," AIAA Journal, **17**, 1293–313
[30] Deardorff J. W., 1970. "A numerical study of three-dimensional turbulent channel flow at large Reynolds numbers," Journal of Fluid Mechanics, **41**, 453–480
[31] Schumann U., 1975. "Subgrid-scale model for finite difference simulation of turbulent flows in plane channels and annuli," Journal of Computational Physics, **18**, 376–404.
[32] Grotzbach G., 1987. "Direct numerical and large eddy simulation of turbulent channel flows," In Encyclopedia of Fluid Mechanics, ed. NP Cheremisinoff, 1337–91. West Orange, NJ: Gulf Publ.
[33] Werner H., and Wengle H., 1993. "Large-eddy simulation of turbulent flow around a cube in a plane channel," In Selected Papers from the 8th Symposium on Turbulent Shear Flows.
[34] Piomelli U., Moin P., Ferziger J., and Kim J., 1989. "New approximate boundary conditions for large-eddy simulations of wall-bounded flows", Physics of Fluids A, **101**, 61–68.

[35] Hoffmann, G., and Benocci, C., 1995. “Approximate wall boundary conditions for large-eddy simulations,” In: Benzi, R. (Ed.), Advance in Turbulence V, 222–228.
[36] Temmerman L., Leschziner M. A., and Hanjalic K., 2002. “A-priori studies of a near-wall RANS model within a hybrid LES/RANS scheme,” In: Rodi, W., Fueyo, N. (Eds.), Engineering Turbulence Modelling and Experiments, Elsevier, 317–326.
[37] Spalart P. R., Jou W. H., Strelets M., and Allmaras S. R., 1997. “Comments on the feasibility of LES for wings and on a hybrid RANS/LES approach,” Advances in DNS/LES, 137–48, Columbus, OH, Also, In Proceedings of the first AFSOR International Conference on DNS/LES, Louisiana Tech University, Aug 4-8, 1997. Gryden Press.
[38] Nikitin N. V., Nicoud F., Wasistho B., Squires K. D., and Spalart P. R., 2000. “An approach to wall modelling in large-eddy simulations,” Physics of Fluids Letters, **12**, 1629-1632.
[39] Viswanathan A. K., and Tafti D. K., 2006. “Detached eddy simulation of turbulent flow and heat transfer in a two-pass internal cooling duct,” International Journal of Heat and Fluid Flow, **27(1)**, 1-20
[40] Baggett J. S. 1998. “On the feasibility of merging LES with RANS in the near-wall modeling in large-eddy simulations,” In: Annual Research Briefs, Center for Turbulence Research, Stanford, CA, 267-277.
[41] Balaras E., and Benocci C., 1994. “Subgrid-scale models in finite-difference simulations of complex wall bounded flows,” AGARD CP 551, 2.1–2.5, Neuilly-Sur-Seine, France: AGARD.
[42] Balaras E., Benocci C., and Piomelli U., 1996. “Two layer approximate boundary conditions for large-eddy simulations,” AIAA Journal, **34**, 1111–1119.
[43] Cabot W., and Moin P., 1999. “Approximate wall boundary conditions in the large eddy simulation of high Reynolds number flow,” Flow, Turbulence and Combustion, **63**, 269–291.
[44] Wang M., and Moin, P., 2002. “Dynamic wall modelling for large-eddy simulation of complex turbulent flows,” Physics of Fluids, **14 (7)**, 2043–2051.
[45] Tessicini F., Li N., and Leschziner M. A., 2007. “Large-eddy simulation of three-dimensional flow around a hill-shaped obstruction with a zonal near-wall approximation,” International Journal of Heat and Fluid Flow, **28**, 894-908.
[46] Germano M., Piomelli U., Moin P., and Cabot W. H., 1991. “A dynamic subgrid-scale eddy viscosity model,” Physics of Fluids A, **3**, 1760-1765.
[47] Lilly D. K., 1992. “A proposed modification of the Germano subgrid scale closure method,” Physics of Fluids, **A4**, 633-635.
[48] Kays W. M., 1992. “Turbulent Prandtl number – where we are?,” Max Jacobs Memorial Award Lecture, 1-12.
[49] Tafti D. K., 2001. “GenIDLEST—A scalable parallel computational tool for simulating complex turbulent flows,” In: Proceedings of the ASME Fluids Engineering Division, FED, ASME-IMECE, November 2001, New York, **256**.
[50] Tafti D. K., 2010. “Time-accurate techniques for turbulent heat transfer analysis in complex geometries, Advances in Computational Fluid Dynamics and Heat Transfer;” Eds: Ryo Amano & Bengt Sunden, Series: Developments in Heat Transfer, WIT PRESS, Southampton, UK, in press.
[51] Moser R., Kim J., and Mansour N., 1999, “Direct numerical simulation of turbulent channel flow up to Re_τ = 590,” Physics of Fluids, **11(4)**, 943-945.
[52] Patil S. S., and Tafti D. K., 2011. “Wall modeled large eddy simulation of high Reynolds number flows,” to appear in Proceedings of AIAA Aerospace Science Meeting, Paper No. 896435.
[53] Wilcox D. C., “Turbulence modeling for CFD,” DCW industries, Second edition.
[54] Incropera F. P., and DeWitt D. P., “Fundamentals of heat and mass transfer,” Wiley Publications, Fifth edition

